Analysis of Superconductors and Metals Using Small-Angle X-ray and Neutron Scattering

Hirokazu Sasaki [*1], *Satoshi Yamazaki* [*1], *Yojiro Oba* [*2], *Masato Onuma* [*3]

ABSTRACT Small-Angle X-ray (SAXS) and Small-Angle Neutron scattering (SANS) were used to analyze metallic nanoparticles, artificial pins in high-temperature superconducting wires, and precipitates of copper alloys. Small-angle scattering provides an average information on the size, the shape and the spacing of these finely dispersed nanoscale structures. In order to ensure the validity of the SAXS or SANS profile analysis, it is necessary to make complementary use of real-space observation techniques such as TEM and 3-D atom probe. This paper illustrates several cases of their use.

1. INTRODUCTION

This paper details Small-Angle X-ray and Small-Angle Neutron Scattering analysis for the development of high-temperature superconducting wires and metallic materials. There are various factors that determines the critical current density in magnetic fields, which is a typical product characteristic of superconducting wires, such as the orientation of superconducting crystals, the formation of normal-conductive phases, and the artificial pins that trap magnetic flux quanta. Among these factors, the fabrication of artificial pins that are formed in the form of rods of a few nm in diameter as designed is important for the production and development of superconducting wires with a high critical current density in magnetic fields.

On the other hand, in order to put many metal materials, including copper alloys, into practical use, it is necessary to improve their material properties such as strength, electrical conductivity, thermal conductivity and workability. There are various factors that govern these characteristics. In particular, strength can be improved by finely dispersing precipitates as small as several nanometers to several tens of nanometers.

As described above, in order to utilize superconducting wires and metal materials, it is important to appropriately finely disperse nano-order structures of several nanometers to several tens of nanometers. Then, it is necessary to analyze whether these structures are formed appropriately not only at the product development stage but also at the manufacturing stage. A typical analysis method is Transmission Electron Microscopy (TEM), which has a spatial resolution of 1 Å or less. Using TEM, you can actually observe and understand the size and shape. However, with TEM, the number of structures that a person can analyze one by one is actually only a few hundred at most, so statistically significant differences may not be found between multiple samples. In this case, Small-Angle X-ray Scattering (SAXS), which can quantitatively evaluate the size and shape of finely dispersed structures, is effective. In addition, a variety of information can be obtained by complementary use of Small-Angle Neutron Scattering (SANS)[1)-7)]. None of these methods is the most effective, but by combining and considering multiple analytical data, it is possible to grasp the essence of nano-order structures. This paper presents analysis examples that use real space analysis methods such as TEM and three-dimensional atom probes in a complementary manner with SAXS and SANS.

[*1] Sustainable Technology Laboratory, R&D Division
[*2] Toyohashi University of Technology
[*3] Hokkaido University

2. SMALL-ANGLE X-RAY AND SMALL-ANGLE NEUTRON SCATTERING

2.1 Small-Angle X-ray Scattering

The experimental setup of SAXS is simple. As shown in Figure 1(a), the sample is irradiated with X-rays, and the X-rays scattered at low angles are detected by a two-dimensional detector. Figure 1(b) shows a scattering image from copper containing precipitates, and the scattering can be clearly detected. Next, the scattering image is circularly integrated to create a SAXS profile. When comparing this SAXS profile between a copper alloy containing precipitates and pure copper without precipitates, as shown in Figure 1(c), a shoulder can be clearly seen in the sample containing precipitates. In this figure, the vertical axis of the SAXS profile is the scattering intensity $I(q)$ and the horizontal axis is the absolute value of the scat-

tering vector q. The SAXS profile is shown as a double-logarithmic graph. By analyzing this intensity profile, information on particle shape, size, number density, and composition can be obtained. In general, profile $I(q)$ can be expressed by equation (1)[2)-7)]. Where, $\Delta\rho$ is the scattering length density difference for X-rays, $N(r)$ is the number density distribution, $V(r)$ is the volume of the particle, and $F(q,r)$ is the shape factor. The scattering length density difference $\Delta\rho$ is the difference between the scattering length density of finely dispersed particles and that of the matrix phase.

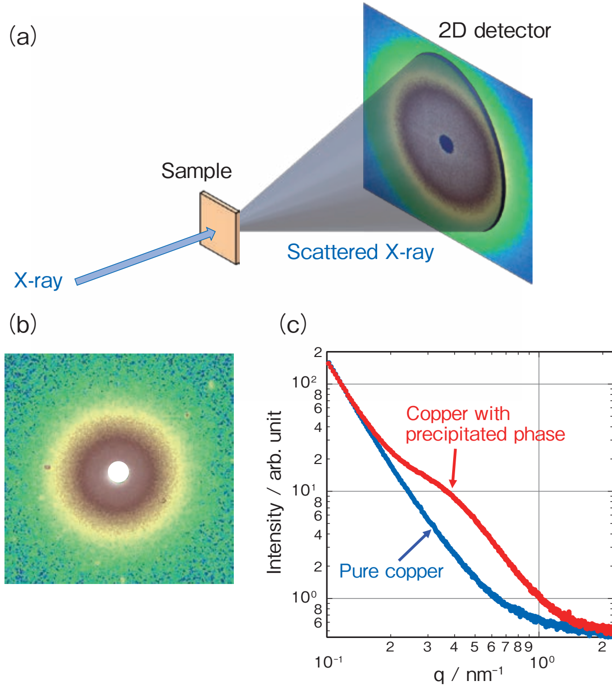

Figure 1 **Schematic diagram of small-angle X-ray scattering and obtained data.**

$$I(q) = \Delta\rho^2 \int_0^\infty N(r)V^2(r)F^2(q,r)\mathrm{d}r \qquad (1)$$

The shape factor F depends on the shape of the particle. Spheres, core-shell structures, ellipsoids, cylinders, and disks have been formulated by previous studies[8)]. For the simplest spherical particles, the shape factor F can be expressed by Equation (2). Where r is the radius of the sphere.

$$F(q,r) = \frac{3\{\sin(qr) - qr\cos(qr)\}}{(qr)^3} \qquad (2)$$

Thus, it is possible to obtain the theoretical scattering intensity from these equations. For example, for a spherical particle whose volume-weighted frequency distribution $N(r){\cdot}V(r)$ follows a lognormal distribution as shown in Figure 2(a), the scattering curve calculated using the analysis software Irena[7)] with Equation (1) is shown in Figure 2(b). One of the characteristics of this profile is that the slope of the curve after the shoulder decreases in proportion to q^{-4}. It is known that the slope depends on the shape of the particle. For cylinders, it decreases in proportion to q^{-1}, and for disks, it decreases in proportion to q^{-2} [8)]. This means that the shape of the particle can be estimated based on what power of q the slope is based on.

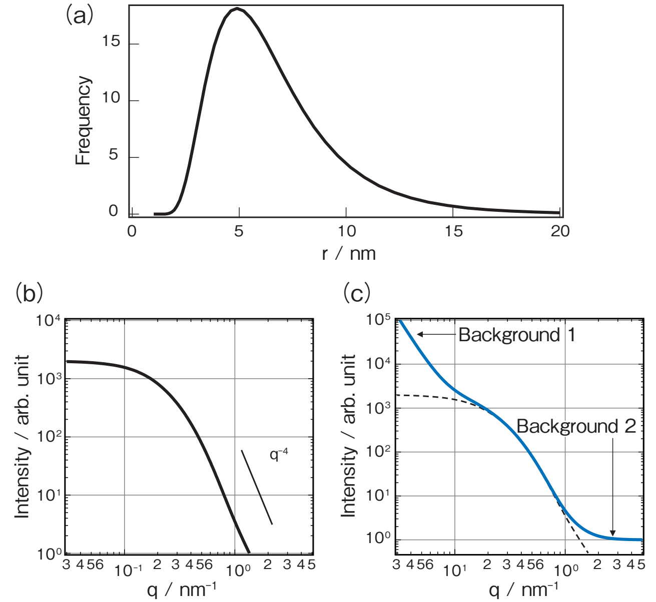

Figure 2 **Calculated SAXS profiles.**

When determining the particle size distribution from the measured SAXS profile, curve fitting is performed from the measured data. In this case, fitting is performed under several assumptions. For example, particles are assumed to be spherical, and the volume-weighted frequency distribution is assumed to be a lognormal distribution that can be expressed by the equation (3). Then the distribution which is the most suitable for measured SAXS profile is obtained where a, σ, and r_0 are constants.

$$N(r)\cdot V(r) = \frac{a}{\sqrt{2\pi}\sigma r}\exp\left[-\frac{\{\ln(r)-\ln(r_0)\}^2}{2\sigma^2}\right] \qquad (3)$$

Therefore, the distribution obtained by fitting from SAXS is not the true distribution of particle sizes, but an interpreted distribution based on the assumptions used in the fitting.

In SAXS measurements of metallic materials, it is rare to obtain only a clear scattering curve as shown in Figure 2(b), and various backgrounds are superimposed in actual measurements. Figure 2(c) shows a typical SAXS profile that is often seen in practice. In this figure, the dashed line represents the profile due to scattering from particles, and the solid line represents the profile including the backgrounds. There are mainly two types of backgrounds. Background 1 is derived from coarse structures, which is noticeable on the low-q side. Incoherent scattering-derived background 2 that appears in the high-q region above q = 2 nm^{-1} also often appears. For these backgrounds, SAXS measurements of samples containing only the matrix phase without fine structures should be performed to determine the background trends, and the effects of these backgrounds should be taken into account in the fitting process. It should be noted, howev-

er, that incoherent scattering is slightly different between the case with only the matrix and the case with microstructures.

Another important factor to keep in mind when measuring metals and superconductors is the X-ray transmittance. In the case of a SAXS system with a Cu source that uses X-rays with an energy of 8 keV, which is widely used in the field of soft matters, metallic materials such as steel, which have a low X-ray transmittance, require grinding to a thickness of 10 μm or less to make the sample thinner and making the sample preparation extremely difficult. On the other hand, if the SAXS system uses a Mo source that produces X-rays with an energy of 17 keV, the X-rays can penetrate sufficiently if the sample is 20 to 30 μm thick, making the sample preparation at a realistic level of difficulty. Another option is to perform SAXS measurements using a high-energy X-rays at synchrotron radiation facilities such as SPring-8.

2.2 Small-Angle Neutron Scattering

While basic principle is the same as that of SAXS, the difference is that a neutron beam is used in this case. Among the several features of SANS, it is noteworthy that neutrons have a strong ability to penetrate materials and can measure thick samples. In the case of metals, it is possible to measure in thicknesses from several millimeters to several centimeters. In many cases, SANS does not require trimming of the specimens, but rather stacking as many specimens as possible to increase the scattering intensity. In addition, the fact that no pretreatment is required is an advantage when the material is soft and difficult to grind. In which case, SANS is more suitable than SAXS.

The difference between SAXS and SANS is not only in the penetration power and the presence or absence of pretreatment, but also in the measurement volume. SAXS measurements require the metal sample to be made thin on the order of μm, meaning that only a small portion of the material is being measured. SANS can measure samples even several millimeters thick, so the measurement volume is 100,000 to 1,000,000 times larger than SAXS. The size of the measured volume is important for practical material evaluation methods, and if it is large enough, the correlation between material properties and finely dispersed structures may be better understood.

Another major motivation for using SANS is that, as shown in Figure 3, the scattering length of neutrons is not proportional to the atomic number like the scattering length of X-rays. That is, the scattering length density difference $\Delta\rho$ in equation (1) is different from that of X-rays. By utilizing this difference in the scattering length density of neutrons and X-rays, that is, the contrast difference, it is also possible to obtain information such as the composition and density of the precipitates.

Because SANS uses neutrons, facilities that can measure it are limited. Representative facilities in Japan are J-PARC and JRR3, each of which has multiple SANS beamlines. In addition, Kyoto University's research reactor KUR, Hokkaido University, and RIKEN have small neutron sources that can be used for SANS.

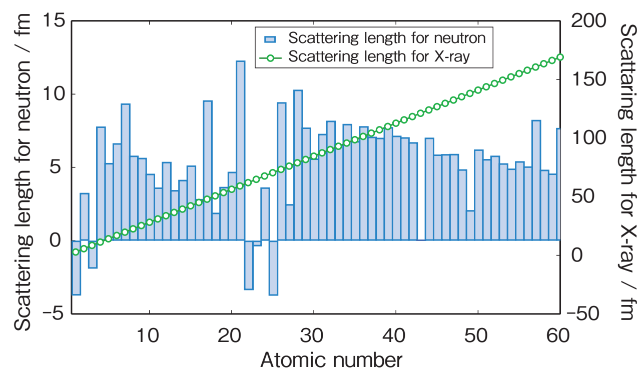

Figure 3 Scattering length of X-ray and neutron beam.

2.3 Complementary Use of TEM and SAXS

While there are many options for analyzing finely dispersed nanoscale structures, TEM, which is a widely used and real-space analysis method, is generally used first. On the other hand, the results obtained by SAXS are average information, but if the average information is the dominant factor in material properties, SAXS is also effective as an analysis method for nano-scale structures.

A brief comparison of the differences in measurement volume between SAXS and TEM is as follows. As shown in Figure 4(a), in the case of SAXS, if the X-ray beam diameter is 100 μm and the sample thickness is 20 μm, the measurement volume is 157,000 μm^3. On the other hand, in TEM, as shown in Figure 4(b), if one side of the observation field is 0.1 μm and the TEM sample thickness is 0.02 μm, the measurement volume is 0.0002 μm^3. Thus, the measurement volume of SAXS is about 9 digits larger than that of TEM, indicating that average information can be obtained. Therefore, using SAXS may make it easier to obtain correlations with material properties. On the other hand, since only the profile shown in Figure 1(c) can be obtained from SAXS, analysis is often difficult from SAXS data alone. Generally, when analyzing a SAXS profile, it is necessary to understand information such as shape through real-space observations such as TEM, so it is important to use SAXS and TEM in a complementary manner for analysis.

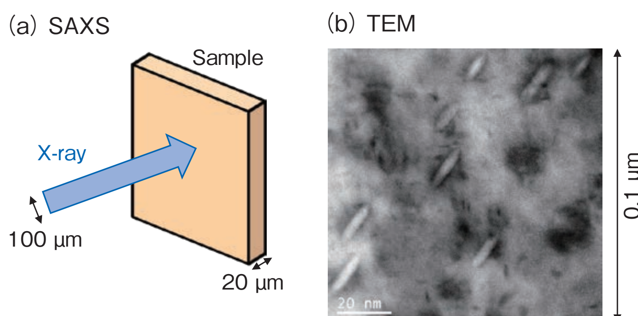

Figure 4 Measurement volumes of SAXS and TEM.

Depending on the material, it is often possible to discuss using TEM alone. For example, assume that the size and shape of finely dispersed structures are relatively uniform, and there is no large difference in particle size no matter which field of view is observed with TEM, as shown in Figure 5(a). In this case, by measuring the size from the TEM image and estimating the particle size distribution, a sufficient correlation with the material properties can be obtained.

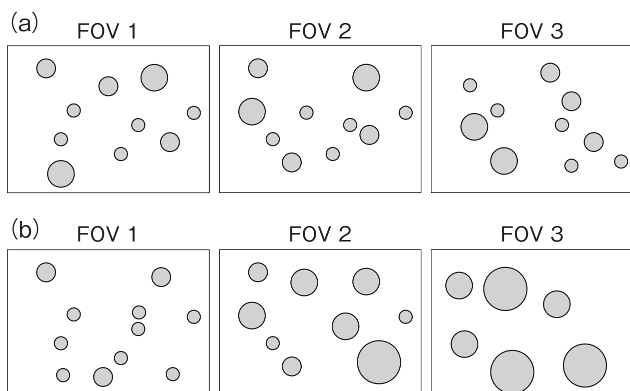

Figure 5 Schematic of particles observed by TEM.

On the contrary, it is difficult to obtain an accurate particle size distribution from the TEM image alone when the size of the structure varies depending on the field of view, as shown in Figure 5(b). Let us consider a case in which small-sized particles are observed in field of view 1, particles of medium size are observed in field of view 2, and relatively large particles are observed in field of view 3. When the particle size distribution is obtained from the particle images observed in these three fields of view and the average particle size is calculated, it is not always correct. Even if one hundred fields of view were observed, such a number would not be enough. The results of the average particle size will differ if there happen to be many fields of view in which particles with large diameters are present, or if there are many fields of view in which particles with small diameters are present. When the particle size varies greatly depending on the field of view, SAXS which has measurement volume several orders of magnitude larger, is effective.

Even if the difference in particle size distribution is small, SAXS is still effective when the difference has a large effect on material properties. TEM can realistically measure only a few hundred particles, and differences between samples may not be detected unless the number of particles is measured several orders of magnitude larger. For example, when considering three volume-weighted frequency distributions as shown in Figure 6(a) for spherical particles, SAXS simulations show different shoulder positions as shown in Figure 6(b), and the differences between them can be detected. In order to capture this difference with TEM, it is necessary to measure as many particles as possible, but this is often difficult in practice.

As described above, when analyzing a finely dispersed structure, depending on the target material, TEM alone may be sufficient in some cases, while SAXS alone may be sufficient if the geometry of the structure is known. In other cases, it may be desirable to use both TEM and SAXS for the analysis.

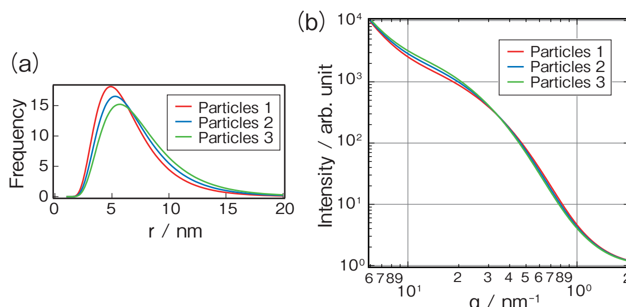

Figure 6 SAXS profiles from various distributions of radii.

3. MEASUREMENT RESULTS

3.1 Metal Nanoparticles

Nanoscale metal particles were fabricated under multiple manufacturing conditions and SAXS measurements were performed to analyze particle size. The measurements were performed at BL8S3, one of the beamlines of Aichi Synchrotron, a synchrotron radiation facility. The energy of the X-rays used in the experiment was 8.2 keV. The camera length, which is the distance between the detector and the sample, was selected to be 1 m and 6 m, and the results of each measurement were connected to produce a single SAXS profile. SAXS profiles of two samples prepared under different manufacturing conditions are shown in Figure 7(a). As indicated by the arrows, shoulders from the metal particles were observed in both samples. Note that because this sample contains large structures, a coarse structure-derived background with a slope of q^{-4} also appears in the low-q region below q = 0.1 nm^{-1}. The background appearing in the high-q region above q = 2 nm^{-1} is due to incoherent scattering and atmospheric effects. From these SAXS profiles, it can be seen that the shoulder of the particles produced under condition A is located on the left side of the graph, i.e., on the low-q side, compared to the shoulder of the particles pro-

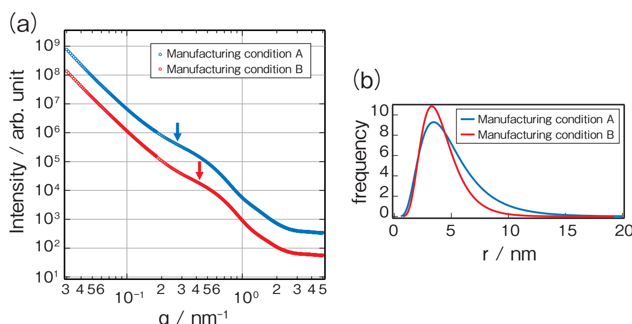

Figure 7 SAXS profiles of metal nanoparticles and their radius distribution.

duced under condition B. Since q as the absolute value of the scattering vector corresponds to the inverse of the real space distance, the appearance of a shoulder at a smaller q implies that the scattering is from a larger structure. These two SAXS profiles indicate that the metallic particles produced under condition A are larger than those produced under condition B. Thus, the average information of the particles can be read from the SAXS profiles alone, and can be used for optimization of production conditions and quality control.

Next, assuming that the metal particles are spherical and the volume-weighted frequency distribution follows a lognormal distribution, curve fitting was performed from these SAXS profiles. The results are shown in Figure 7(b). Although there is no significant difference in the peak position of the distribution between the two samples, the distribution for condition A has a tail in the region of larger diameter, indicating that there are many particles that are larger than those in condition B. This means that the particles in condition A have a larger variation in particle size. In this case, r_0 in the log-normal distribution is 4.5 nm for the metal particles fabricated under condition A and 3.9 nm for the metal particles fabricated under condition B, so larger particles are formed under condition A. Thus, the particle size can be analyzed from the SAXS profile and the results can be fed back to the manufacturing conditions to optimize the particle size.

3.2 Superconducting Wires[9)]

To develop high current density materials, it is necessary to appropriately control magnetic flux quanta. That is the proper pinning of the magnetic flux quanta in the normal conducting parts (pins). Challenges in the development of superconducting wires arise when the causal relationship between physical properties and superconducting thin film structures such as pinning centers is not fully understood. Controlling pinning center is difficult because the factors that generate it are complex, such as twins and oxygen deficiency. Therefore, rods with several nm in diameter are artificially fabricated perpendicular to the superconducting film[10)-13)]. The diameters and density of the artificial pins are the main factors determining the critical current density of superconducting wires. If the artificial pins can be introduced as designed, the superconducting phase can be maintained even in high magnetic fields, and wires with high critical current density in magnetic fields can be realized.

Against this background, it is important for high-quality superconducting wires to conduct material analysis to determine whether the artificial pins are fabricated as designed. TEM observation is commonly used to analyze artificial pins. However, the observation area is small, a few μm range, and may not be sufficient for quantitative evaluation of the size distribution of artificial pins over the entire wire. In response to these requests, we analyzed nanorod artificial pins using SAXS. The sample used was a GdYBCO superconducting wire with Zr added to form $BaZrO_3$ artificial pins. The composition of the superconducting layer is approximately $(Gd,Y)_1Ba_2Cu_3O_7$, and the thickness of the superconducting layer is 2 μm. A crystal orientation-controlled intermediate layer was laminated on Hastelloy with a thickness of approximately 50 μm, and a superconducting layer containing artificial pins was deposited on the top of this. Figure 8(a) shows a TEM image of the artificial pins observed from a direction perpendicular to the surface of the superconducting thin film. It can be seen that artificial pins with a diameter of several nanometers are formed. Figure 8(b) shows a HAADF (High Angle Annular Dark Field) - STEM (Scanning Transmission Electron Microscopy) image of a magnified image of a part of the GdYBCO. It can be seen that the artificial pins and GdYBCO are partially bonded and stably formed. Figure 8(c) shows a TEM image of the artificial pins observed from the cross-sectional direction of the superconducting thin film. Rod-shaped artificial pins are formed in the growth direction of the thin film.

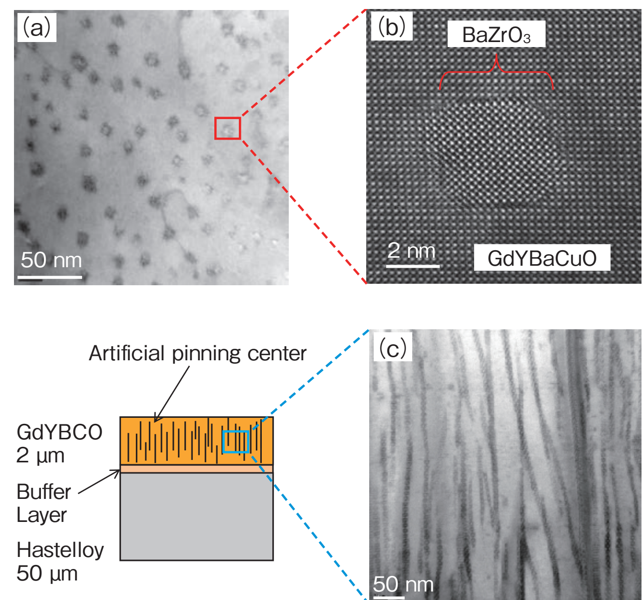

Figure 8 TEM images of artificial pins in superconducting wire.

Although there is a previous study of SAXS analysis of artificial pins in superconducting thin films using Au artificial pins[14)], it was expected to be difficult for $BaZrO_3$ artificial pins because the contrast between the electron density of the base phase $(Gd, Y)_1Ba_2Cu_3O_7$ and $BaZrO_3$ artificial pins is small. Furthermore, superconducting wires have nanoscale structures other than the artificial pins, which may also provide scattering. In addition, the scattering from the substrate Hastelloy provides a background that affects the scattering of the artificial pins. Therefore, artificial pin evaluation was performed using Anomalous Small-Angle X-ray Scattering (ASAXS) using the Zr absorption edge. ASAXS can selectively capture scattering from $BaZrO_3$ artificial pins containing Zr because the atomic scattering factor changes as the incident energy approaches the Zr absorption edge.

The experiment was conducted at beamline BL19B2 of SPring-8. SAXS measurements were performed by

arranging the samples so that X-rays were transmitted in the direction of growth of the superconducting thin films to investigate the in-plane nanostructures. ASAXS measurements were performed at incident energies of –3 eV, –8 eV, –13 eV, and –113 eV away from the Zr absorption edge. As a preliminary experiment, we conducted XANES measurements of ZrO_2 powder and performed energy calibration assuming that the Zr-K absorption edge was 17.998 keV[15]. The camera length was 3040 mm, and the measurements were performed in the region where the q value was approximately 0.06 to 3.5 nm^{-1}. The scattering intensity was calibrated at each energy using glassy carbon as a standard sample[16].

Figure 9(a) shows the Anomalous Small-Angle X-ray Scattering results of a $(Gd,Y)_1Ba_2Cu_3O_7$ thin film with 25% Zr added. A shoulder was observed near q = 0.2-1.0 nm^{-1}, confirming the formation of nanostructures of several tens of nanometers in the superconducting layer. Compared to the profile of –113 eV, which is sufficiently far from the absorption edge, the –3 eV, –8 eV, and –13 eV profiles have increased peak intensities around q = 0.3 nm^{-1}. This suggests that these peaks are scattering derived from artificial pins of $BaZrO_3$ containing Zr.

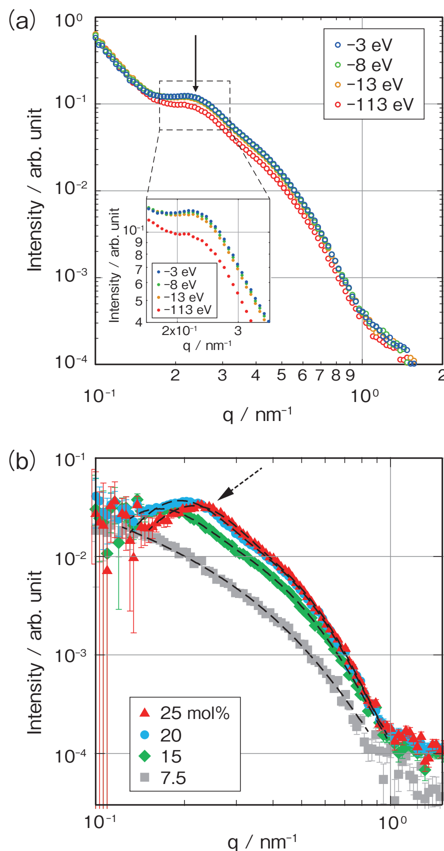

Figure 9 ASAXS profiles of artificial pins in superconductor.

Figure 9(b) shows the results of subtracting the –113 eV profiles from the –3 eV profiles. The measured samples contained 7.5%, 15%, 20%, and 25% Zr. The scattering profiles of $BaZrO_3$ have a peak-like feature around q = 0.25 nm^{-1}, as indicated by the arrow in the figure. This may be due to interparticle interference effects, suggesting that the artificial pins are densely packed in the superconducting layer. Curve fittings for these peaks were performed by approximating a Gaussian function and a linear function as the background to estimate the peak position q_{peak}[17]. From the result of the sample containing 25% Zr, the average distance between artificial pins $L = 2\pi / q_{peak}$ was estimated to be 27 nm. The distance between artificial pins, which is closely related to the critical current density, can be quantified using ASAXS measurements. Figure 10(a) shows the results of analysis of samples with Zr addition amounts of 15%, 20% and 25%. Figure 10(a) also shows the density of artificial pins calculated from the distance between pins. It was analyzed that as the Zr concentration increases, the distance between the pins decreases and the density of the artificial pins increases. In addition, for the 7.5 % Zr containing sample, the interference peak did not appear and could not be calculated because the density of the artificial pins was low and the interference effect was weak.

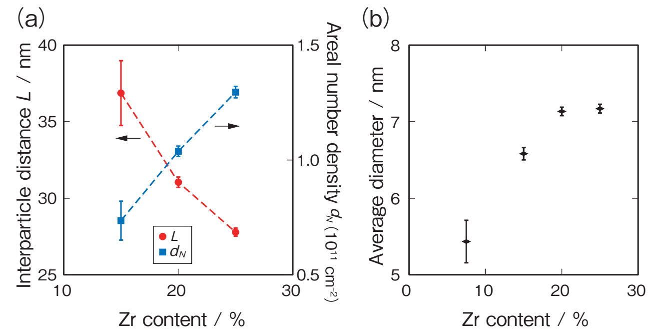

Figure 10 Average structural information analyzed from ASAXS measurement.

To calculate the diameter of the artificial pins, curve fitting was performed assuming an oriented rod model. As the TEM image in Figure 8(c) shows that the rod is slightly tilted with respect to the growth direction of the thin film, the rod tilt was also taken into account in the SAXS fitting. In addition, since a peak appeared, the influence of interparticle interference was also taken into account. The fitting results are shown in Figure 9(b). The average diameters of the artificial pins obtained from these results are shown in Figure 10(b). In this type of samples, the diameters tend to increase as the Zr concentration increases, but it reaches saturation at 20%. As described above, we were able to analyze average information on artificial pin spacing, density, and size using ASAXS. By performing such analyzes appropriately, it becomes possible to develop and manufacture high-quality superconducting wires.

3.3 Copper Alloys[18]

Copper products require strength, electrical conductivity, thermal conductivity, and workability. One of the copper alloys that meet these required properties is Cu-Ni-Si alloy, and it is known that heat treatment improves strength by finely dispersing Ni-Si compounds in the cop-

per matrix. This Cu-Ni-Si alloy is called Corson alloy, and it has both high strength and high electrical conductivity. Today, various Cu-Ni-Si alloys have been developed by adding various additives to improve their properties, and these alloys are widely used in electronic devices such as smartphones, making them indispensable metallic materials in our daily lives.

The sample analyzed was a Cu-Ni-Si alloy containing 2.5 mass% Ni and 0.6 mass% Si. The Cu-Ni-Si alloy was melted and cast, and then heat-treated, rolled, annealed, and solution heat-treated. After that, aging treatment was performed. We analyzed the alloys after samples had been solution heat-treated and heat-treated at aging temperatures of 425, 450, 500 and 550°C. The aging time was 2 h.

Figure 11(a) shows a bright-field TEM image of the Ni-Si precipitate in a Cu-Ni-Si alloy that was heat-treated at 550°C for aging precipitation. The TEM image shows numerous precipitates of about 10 nm in size. The copper matrix surrounding the precipitates shows contrast due to distortion. A magnified HAADF-STEM image of one of the precipitates is shown in Figure 11(b). Analysis of this image with a two-dimensional fast Fourier pattern (details omitted here) revealed that the precipitate was δNi_2Si[19), 20)]. Many previous studies of Ni-Si precipitates by TEM have shown that the precipitates are δNi_2Si[21)-26)] .

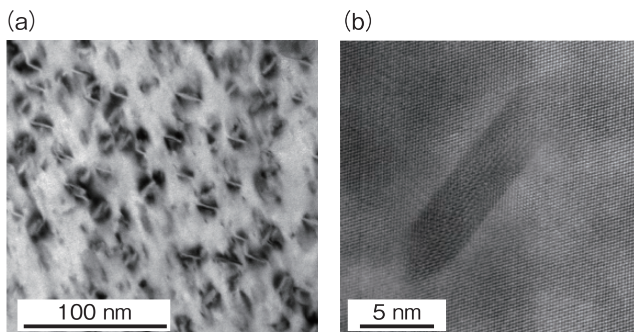

Figure 11 TEM images of precipitate from Cu-Ni-Si alloy.

In order to analyze the structure of the precipitated phase in detail, we used a 3-D atom probe to analyze it. In the 3-D atom probe method, the material is evaporated, the evaporated atoms are detected by a 2-D detector, and the data are reconstructed to visualize the 3-D structure on the nanometer order[27)]. The apparatus used was LEAP5000XS. The measured temperature was 30 K. A pulsed ultraviolet laser with a wavelength of 355 nm was used as the light source to assist evaporation[28)]. Figure 12 shows the analysis results of the sample heat-treated at 550°C. Figure 12(a) shows an iso-concentration surface of 7 atomic% Si. The precipitates were not spherical but ellipsoidal, close to a disk. Figure 12(b) shows the concentration profile of the precipitate created in the direction indicated by the arrow in Figure 12(a). The Ni/Si ratio of 2:1 in the center suggests that the precipitates are Ni_2Si. It can also be confirmed that Ni, Si, and Cu are interdiffused at the interface between the precipitated phase and the copper matrix. By closely observing the diffused area, two characteristics can be found. One is the region indicated by arrow 1, where the Si composition is constant and the Ni composition decreases toward the copper matrix side. This region is considered to be $\delta(Ni_{1-y},Cu_y)_2Si$[29)]. The other region is indicated by arrow 2, where Ni and Si are diffused into the copper matrix at a concentration of 10% or less. Figure 13 shows a model diagram of the precipitates estimated from these TEM and 3-D atom probes. As shown above, it is important to analyze small-angle scattering after understanding the structure and size of the precipitates to some extent through real-space analysis in order to draw a reliable conclusion.

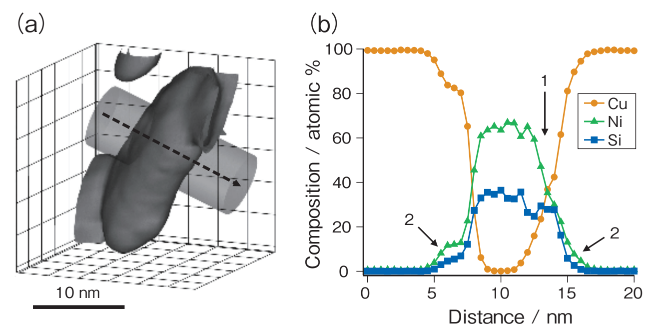

Figure 12 Three-dimensional atom probe result of precipitate.

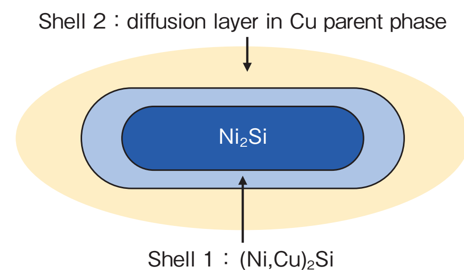

Figure 13 Core-shell model diagram of precipitate.

Rigaku NANO-Viewer was used for SAXS measurements. The Mo-Kα source was used, the incident X-ray energy was 17.47 keV, and the camera length was 0.5 m. Furthermore, Ultra Small Angle X-ray Scattering (USAXS) measurements were performed at SPring-8's Hyogo Prefecture Beamline BL08B2. The incident X-ray energy was 18 keV, and the camera length was 16 m. The sample was trimmed to a thickness of approximately 20 μm. For the laboratory SAXS profile, the absolute value of the strength was calculated using glassy carbon[16)]. The USAXS profiles were connected to the intensity of that SAXS profile to create a single SAXS profile. SANS measurements were performed using SANS-J installed at JRR3[30)]. The sample for SANS measurements was approximately 2.1 mm thick. The measurement results of SAXS and SANS are shown in Figure 14(a), (b). The figure shows small-angle scattering profiles for solution anneal-

ing only and for samples heat-treated at aging temperatures of 425, 450, 500, and 550°C. Compared to the Corson alloy that was only solution treated, the 425°C aging precipitation heat-treated product shows a shoulder indicating the formation of nanoparticles in the region of q = 0.4 to 2 nm^{-1}. It can be observed that the shoulder showing scattering moves to the low-q side as the aging heat treatment temperature increases. These results suggest that the Ni-Si precipitates are gradually coarsening.

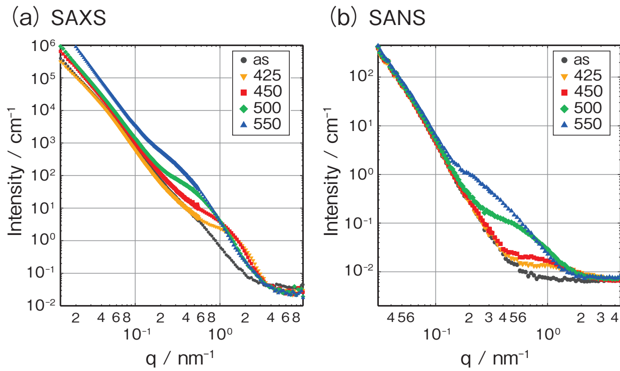

Figure 14 SAXS and SANS profiles of Cu-Ni-Si alloy.

Based on the TEM and 3-D atom probe results of the precipitated phase, the SANS results were analyzed. Figure 15 shows the SANS and SAXS results for the 550°C-aged sample. Since the precipitates of the 550°C aged sample were assumed to be ellipsoids close to disks, the SAXS and SANS profiles were fitted assuming that they were ellipsoids. The axis ratio of the ellipsoid was assumed to be 0.3. In this fitting, the background derived from incoherent scattering that appears in the high-q region of approximately q = 2 nm^{-1} or more is set to a constant value, and the coarse structure-derived background that becomes prominent in the low-q side was taken as q^{-4}.

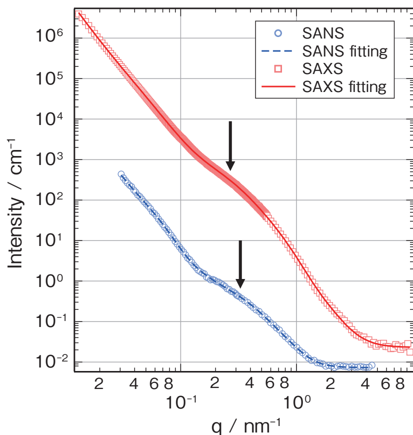

Figure 15 SAXS and SANS profiles of 550°C aging samples.

The fitting results are shown by solid and dashed lines in Figure 15. The shoulder near q = 0.3 nm^{-1}, indicated by the arrow in the figure, corresponds to the precipitates.

As a result of fitting with the SAXS profile, the average major axis radius of the ellipsoid was 8.9 nm. On the other hand, the average major axis radius of the ellipsoid fitted with the SANS profile was 6.6 nm. The reason for the difference in results between SAXS and SANS is the difference in scattering contrast of the diffuse layer of $\delta(Ni_{1-y},Cu_y)_2Si$, in which Cu diffuses into the precipitated phase. Figure 16 shows the results of calculating the scattering contrast of the $\delta(Ni_{1-y},Cu_y)_2Si$ diffusion layer based on the X-ray and neutron scattering lengths shown in Figure 3. From these results, the scattering contrast of the $\delta(Ni_{1-y},Cu_y)_2Si$ diffusion layer in the copper matrix is large for X-rays but small for neutrons. Therefore, it is considered that the precipitated phase was measured large in SAXS and small in SANS. By using SAXS and SAXS in a complementary manner in this way, it is possible to quantitatively analyze the average size of precipitates, taking into account the diffusion layer. In practice, product development is conducted based on the correlation between such analysis results and material properties such as strength and electrical conductivity.

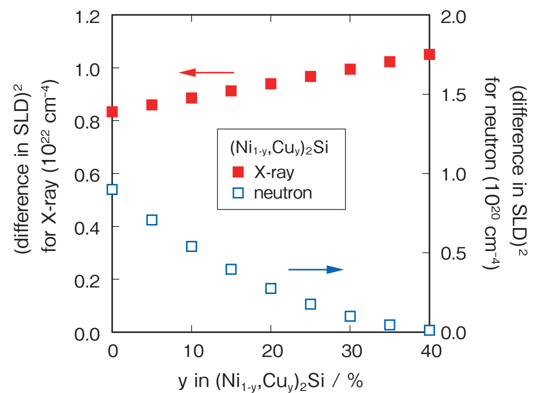

Figure 16 X-ray and neutron contrast of $\delta(Ni_{1-y},Cu_y)_2Si$ diffusion layer in copper.

4. CONCLUSION

In this paper, we have shown that SAXS and SANS are useful for the analysis of finely dispersed nanoscale structures such as metallic nanoparticles, artificial pins in high-temperature superconducting wires and precipitates in copper alloys. Complementary use of real-space observation techniques, such as TEM and 3-D atom probe, enables analysis of reasonable small-angle scattering profiles. There are many materials analysis techniques other than those illustrated in this paper, and it is important to discuss them based on the results of appropriately combining multiple methods. We plan to continue using this technology in the development of various new products and in ensuring the reliability of various existing products.

ACKNOWLEDGMENTS

The laboratory-based SAXS measurements of copper alloys were performed under the collaboration of the Institute for Integrated Radiation and Nuclear Science, Kyoto University. SPring-8 ASAXS measurements of superconductivity were performed at BL19B2 (Proposal No. 2016B1790). SAXS measurements of copper alloys at SPring-8 were performed at the Hyogo Prefecture Beamline BL08B2 (Proposal No. 2019A3337), and SANS measurements were performed at the SANS-J of the JAEA JRR3 (Proposal No. 2021A-A43). The HAADF-STEM observation was supported by the University of Tokyo Advanced Characterization Nanotechnology Platform in the Nanotechnology Platform Project sponsored by the Ministry of Education, Culture, Sports, Science and Technology of Japan. 3-D atom probe measurement of copper alloys was performed with the cooperation of Dr. Jun Uzuhashi, Dr. Kyoko Suzuki, and Dr. Tadakatsu Okubo of the National Institute for Materials Science.

REFERENCES

1) Yojiro Oba: Bulletin of the Iron and Steel Institute of Japan (In Japanese), 18 (2013), 257.
2) Masato Onuma: Materia (In Japanese), 54 (2015), 616.
3) Masato Onuma: Surface Science (In Japanese), 33 (2012), 278.
4) M. Ohnuma, J. Suzuki, S. Ohtsuka, S. W. Kim, T. Kaito, M. Inoue and H. Kitazawa: Acta Mater., 57 (2009), 5571.
5) Y. Oba, S. Koppoju, M. Ohnuma, T. Murakami, H. Hatano, K. Sasakawa and A. Kitahara, J. Suzuki: ISIJ Int., 51 (2011), 1852.
6) T. Tanaka, Y. Taji, P. Pawel Kozikowski, M. Onuma, M. Nagano: Iron and Steel (In Japanese), 105, 10 (2019), 25.
7) J. Ilavsky and P. Jemian, : J. Appl. Cryst., 42 (2009), 347.
8) J. S. Pedersen: Adv. Colloid. Interfac., 70 (1997), 171.
9) Y. Oba, H. Sasaki, S. Yamazaki, R. Nakasaki, and M. Ohnuma, Supercond. Sci. Technol., 32 (2019), 05501.
10) J. L. MacManus-Driscoll, S. R. Foltyn, Q. X. Jia, H. Wang, A. Serquis, L. Civale, B. Maiorov, M. E. Hawley, M. P. Maley and D. E. Peterson, Nat. Mater., 3 (2004), 439.
11) Y. Yamada, K. Takahashi, H. Kobayashi, M. Konishi, T. Watanabe, A. Ibi, T. Muroga, S. Miyata, T. Kato, T. Hirayama and Y. Shiohara, Appl. Phys. Lett., 87 (2005), 132502.
12) S. Kang, A. Goyal, J. Li, A. A. Gapud, P. M. Martin, L. Heatherly, J. R. Thompson, D. K. Christen, F. A. List, M. Paranthaman and D. F. Lee: Science, 311(2006), 1911.
13) V. Selvamanickam, Y. Chen, T. Shi, Y. Liu, N. D. Khatri, J. Liu, Y. Yao, X. Xiong, C. Lei, S. Soloveichik, E. Galstyan and G. Majkic: Supercond. Sci. Technol., 26 (2013), 035006.
14) T. Horide, K. Matsumoto, H. Adachi, D. Takahara, K. Osamura, A. Ichinose, M. Mukaida, Y. Yoshida and S. Horii: Physica C, 445 (2006), 652.
15) P. Li, I-W. Chen and J. E. Penner-Hahn: Phys. Rev. B, 48 (1993), 10063.
16) F. hang, J. Ilavsky, G. G. Long, J. P.G. Quintana, A. J. Allen and P. R. Jemian: Metall. Mater. Trans., 41A (2010), 1151.
17) S. Förster, A. Timmann, M. Konrad, C. Schellbach and A. Meyer: J. Phys Chem. B, 109 (2005), 1347.
18) Hirokazu Sasaki, Shunta Akitani, Kuniteru Mihara, Yojiro Oba, Masato Onuma, Jun Uzuhashi, Tadakatsu Okubo: Copper and Copper Alloys (In Japanese), 62, 1 (2023), 85.
19) Hirokazu Sasaki, Shunta Akitani, Yojiro Oba, Masato Onuma, A. D. Giddings, Tadakatsu Okubo: Copper and Copper Alloys (In Japanese), 60 ,1 (2021), 309.
20) H. Sasaki, S. Akiya, Y. Oba, M. Onuma, A.D. Giddings and T. Ohkubo: Mater. Trans., 63 (2022), 1384.
21) S. A. Lockyer and F. W. Noble: J. Mater. Sci., 29 (1994), 218.
22) Hidemichi Fujiwara, Tatsuo Sato, Akihiko Kamio: Journal of the Japan Institute of Metals (In Japanese), 62 (1998), 301.
23) Akiyoshi Araki, Ikuo Kobayashi, Tatsuo Sato, Kiyoshige Hirose, Tatsuhiko Eguchi: Copper and Copper Alloys (In Japanese), 52 (2013), 14.
24) Q. Lei, Z. Li, C. Dai, J. Wang, X. Chen, J. M. Xie, W. W. Yang and D.L. Chen: Mater. Sci. Eng., A572 (2013), 65.
25) Y. Jia, M. Wang, C. Chen, Q. Dong, S. Wang and Z. Li: J. Alloys Compd., 557 (2013), 147.
26) A. Araki, W. J. Poole, E. Kobayashi and T Sato: Mater. Trans., 55 (2014), 501.
27) Tadakatsu Okubo, Y. Chen, Masaya Kozuka, Kazuhiro Takarano: Materia (In Japanese), 50 (2011), 397.
28) J. Uzuhashi, T. Ohkubo and K. Hono: Ultramicroscopy, 247 (2023), 113704.
29) J. Yi, Y. Jia, Y. Zhao, Z. Xiao, K. He, Q. Wang, M. Wang and Z. Li: Acta Materialia, 166 (2019), 261.
30) T. Kumada, R. Motokawa, Y. Oba, H. Nakagawa, Y. Sekine, C. Michael, Y. Ueda, T. Sugita, A. Birumachi, M. Sasaki, K. Hiroi, and H. Iwase, J. Apple. Crystal., 56 (2023) 1776.